

Origin of asymmetries in X-ray emission lines from the blast wave of the 2014 outburst of nova V745 Sco

Salvatore Orlando^{1*}, Jeremy J. Drake², Marco Miceli^{1,3}

¹*INAF - Osservatorio Astronomico di Palermo “G.S. Vaiana”, Piazza del Parlamento 1, 90134, Palermo, Italy*

²*Harvard-Smithsonian Center for Astrophysics, 60 Garden Street, Cambridge, MA 02138, USA*

³*Dip. di Fisica & Chimica, Università di Palermo, Piazza del Parlamento 1, 90134, Palermo, Italy*

Accepted. Received

ABSTRACT

The symbiotic nova V745 Sco was observed in outburst on 2014 February 6. Its observations by the *Chandra* X-ray Observatory at days 16 and 17 have revealed a spectrum characterized by asymmetric and blue-shifted emission lines. Here we investigate the origin of these asymmetries through three-dimensional hydrodynamic simulations describing the outburst during the first 20 days of evolution. The model takes into account thermal conduction and radiative cooling and assumes a blast wave propagates through an equatorial density enhancement. From the simulations, we synthesize the X-ray emission and derive the spectra as they would be observed with *Chandra*. We find that both the blast wave and the ejecta distribution are efficiently collimated in polar directions due to the presence of the equatorial density enhancement. The majority of the X-ray emission originates from the interaction of the blast with the equatorial density enhancement and is concentrated on the equatorial plane as a ring-like structure. Our “best-fit” model requires a mass of ejecta in the outburst $M_{\text{ej}} \approx 3 \times 10^{-7} M_{\odot}$ and an explosion energy $E_{\text{b}} \approx 3 \times 10^{43}$ erg and reproduces the distribution of emission measure vs temperature and the evolution of shock velocity and temperature inferred from the observations. The model predicts asymmetric and blue-shifted line profiles similar to those observed and explains their origin as due to substantial X-ray absorption of red-shifted emission by ejecta material. The comparison of predicted and observed Ne and O spectral line ratios reveals no signs of strong Ne enhancement and suggests the progenitor is a CO white dwarf.

Key words: shock waves – binaries: symbiotic – circumstellar matter – stars: individual (V745 Sco) – novae, cataclysmic variables – X-rays: binaries

1 INTRODUCTION

V745 Sco is a symbiotic nova that was observed in its latest outburst on 2014 February 6 (Waagen 2014). Previous outbursts were recorded in 1937 and 1989 (Duerbeck 1989) and, probably, one was missed in the 1960s (Schaefer 2010). This makes of V745 Sco a member of the elusive group of recurrent novae (Duerbeck 1989). The characteristics of the V745 Sco stellar system are poorly known due to the crowded galactic bulge region in which it sits; it is thought to be a close binary, comprising a red giant star and a white dwarf (Duerbeck 1989) with an orbital period of 510 ± 10 days, and located at a distance of 7.8 ± 1.2 kpc (Schaefer 2010). In this class of objects, material is trans-

ferred from the companion red giant onto the surface of the white dwarf. The outbursts occur on the white dwarf when the transferred material reaches sufficient temperature and density to trigger a thermonuclear runaway (e.g. Anupama & Mikolajewska 1999; Starrfield et al. 2000).

The 2014 outburst was monitored since the early phases of its evolution by an intensive observing campaign, including observations ranging from radio, to X-ray and γ -ray wavelengths. A summary of the observations is presented in Page et al. (2015). Observations of the *Chandra* X-ray Observatory Transmission Grating Spectrometers on UT 2014 February 22, and 23 (namely between 15.8 and 17.4 days since the outburst) revealed a rich spectrum of emission lines indicative of emitting plasma with temperatures ranging between a few MK and tens of MK (Drake et al. 2016). The spectral analysis has shown that X-ray line profiles are

* E-mail: orlando@astropa.inaf.it

significantly asymmetric and too strongly peaked to be explained by a spherically-symmetric blast wave (Drake et al. 2016); also the lines present a systematic blueshift of $160 \pm 10 \text{ km s}^{-1}$. All these features have been interpreted as evidence of significant blast collimation in analogy with the findings of previous studies of other nova outbursts.

In recent years, there has been a growing consensus in the literature that blast collimation is a common feature of nova outbursts. For instance, collimation signatures analogous to those found for V745 Sco have been found during the 2006 outburst of the recurrent nova RS Oph at radio, infrared, optical, and X-ray wavelengths (e.g. Sokoloski et al. 2006; O’Brien et al. 2006; Bode et al. 2006; Luna et al. 2009; Drake et al. 2009). Convincing theoretical support of the idea that nova blasts are highly collimated has been provided by accurate multi-dimensional hydrodynamic models. These have shown that the interaction of the explosion with either an accretion disc or a disc-like equatorial density enhancement (hereafter EDE) around the white dwarf produces a characteristic bipolar shock morphology in which both the blast and the ejecta from the outburst are strongly collimated in polar directions (e.g. Walder et al. 2008; Orlando et al. 2009; Drake & Orlando 2010; Orlando & Drake 2012; Pan et al. 2015). In the case of the 2006 outburst of RS Oph, Orlando et al. (2009) have shown that the broadening of emission lines observed with *Chandra* is the result of the interaction of the blast wave with an EDE and their asymmetries are due to substantial X-ray absorption of red-shifted emission by ejecta material. Besides that, ascertaining the presence of an EDE in these systems is important also to unveil the origin of γ -ray emission which seems to originate at the interface between the equatorial and polar regions (Chomiuk et al. 2014; Metzger et al. 2015) where, most likely, the blast interacts with the EDE.

In this paper, we explore the effects of the EDE and the red giant companion on the blast wave morphology and ejecta distribution during the 2014 outburst of V745 Sco through hydrodynamic modeling. The aims include: 1) to ascertain the role of the EDE in the collimation of blast wave and ejecta during this particular event; 2) to provide a deeper insight on the origin of the asymmetries, broadening, and blueshifts revealed in the profiles of X-ray emission lines; and 3) to constrain the environment surrounding this binary system by deriving the average density structure and geometry of the circumstellar medium (CSM) immediately surrounding the nova. The latter point may provide important clues on the final stages of stellar evolution. Also it is relevant for our understanding of the origin of non-thermal (synchrotron) emission observed in nova outbursts (e.g. Chomiuk et al. 2014) which is likely due to interaction of blast and ejecta with the dense material of the EDE. In our approach, we synthesize the X-ray emission from the hydrodynamic simulations and derive the spectra as they would be observed with the *Chandra* Transmission Grating Spectrometers; finally we compare the model results with observations. In Section 2 we describe the hydrodynamic model, the numerical setup, and the synthesis of X-ray emission; in Section 3 we discuss the results; and finally in Section 4 we draw our conclusions.

2 HYDRODYNAMIC MODELING

The three-dimensional hydrodynamic model adopted here is similar to that of Orlando et al. (2009) and describes the expansion of the blast wave from the 2014 outburst of the nova V745 Sco through the extended outer atmosphere of the companion red giant. The blast wave is modeled by numerically solving the time-dependent fluid equations of mass, momentum and energy conservation, including the radiative losses from an optically thin plasma and the thermal conduction. The evolution of ejecta is traced by considering a passive tracer, C_{ej} , associated with them (see Orlando et al. 2009 for more details). The calculations are performed using FLASH, an adaptive mesh refinement multiphysics code for astrophysical plasmas (Fryxell et al. 2000). The hydrodynamic equations for compressible gas dynamics are solved using the FLASH implementation of the piecewise-parabolic method (Colella & Woodward 1984).

For the system parameters (namely binary separation, a_{bs} , and radius of the red giant companion, R_*), we adopt the values of Schaefer (2009) (see Table 1). The companion is included as an impenetrable body with radius $R_* = 126 R_{\odot}$. We assume the gas density in the wind is proportional to r^{-2} (where r is the radial distance from the companion red giant) and explore different values of the mass-loss rate. In addition to the r^{-2} density distribution, we include a diffuse, disc-like distribution around the binary system which describes an EDE (see Fig. 1). Detailed hydrodynamic modeling studies predict that this equatorial structure originates from gravitational accumulation of the cool red giant wind towards the white dwarf (e.g. Walder et al. 2008; Pan et al. 2015). Following Orlando & Drake (2012), we describe the mass density distribution of the unperturbed CSM in Cartesian geometry as

$$\rho = \rho_w r_{\text{pc}}^{-2} + \rho_{\text{ede}} e^{[-(x/h_x)^2 - (y/h_y)^2 - (z/h_z)^2]} \quad (1)$$

where $\rho_w = \mu m_{\text{H}} n_w$ is the wind mass density at 1 pc, $\mu \approx 1.3$ is the mean atomic mass (assuming metal abundances of 0.5 times the solar values; Orio et al. 2015), m_{H} is the mass of the hydrogen atom, r_{pc} is the radial distance from the red giant in pc, $\rho_{\text{ede}} = \mu m_{\text{H}} n_{\text{ede}}$ is the density of the EDE close to the red giant, and h_x , h_y , and h_z are characteristic length scales determining the size and shape of the EDE.

Note that, in our description of the CSM, we do not consider the effect of the white dwarf which may induce a wake like a spiral arm due to its orbit through the red giant wind. The V745 Sco system is believed to be quite similar to the RS Oph system (see the discussion at the beginning of section 3.1). Thus, we can estimate the region expected to be dominated by spiral arms from the work of Walder et al. (2008) in which the authors reconstruct the density structure of the pre-nova CSM around RS Oph. From their Fig. 2, we note that the region which is heavily dominated by the arms is within a distance of $\approx 1 \text{ au}$ from the white dwarf. We expect, therefore, that our model (which neglects the more complex structure of the CSM immediately surrounding the white dwarf) does not describe accurately the very early (first day) evolution of the blast. On the other hand, in this work, we aim at comparing our model results with observations at later times ($> 1 \text{ day}$), namely when the blast is expected to propagate through the less perturbed part of the EDE. In particular we do not expect any relevant effect

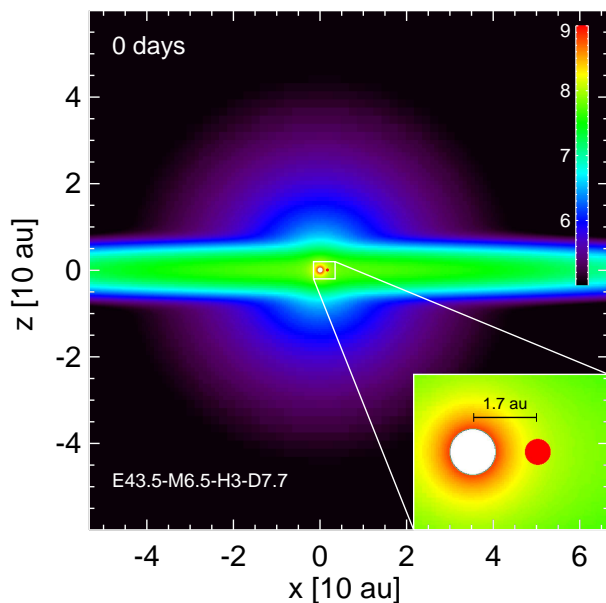


Figure 1. Colour-coded cross-section image of the gas density distribution, on a logarithmic scale, in units of cm^{-3} , showing the initial conditions of run E43.5-M6.5-H3-D7.7. Note that only one quadrant of the whole spatial domain was modeled numerically, namely for positive values of y and z (see text and Table 1). The inset panel shows a close-up view of the initial geometry of the V745 Sco system. The companion star is at the origin (white circle on the left of the inset), and the initial spherical blast wave lies on the x axis at $x = 1.7$ au (red circle on the right).

on the X-ray emission synthesized at day 17, corresponding to the time of *Chandra* observations.

As an initial condition, we assume a spherical Sedov-type blast wave originating from the thermonuclear explosion with total energy E_b and ejecta mass M_{ej} . No wind phase after the initial thermonuclear runaway event is considered (e.g. Kato & Hachisu 1994, 2009). The blast wave is centered on the white dwarf, with an initial radius $r_{b0} = 0.3$ au, offset from the red giant by 1.7 au (Schaefer 2009). The influence of the different system parameters is investigated by exploring models with an initial energy of explosion E_b in the range $10^{43} - 10^{44}$ erg, ejecta mass M_{ej} in the range $10^{-7} - 10^{-6} M_{\odot}$, wind density at 1 pc n_w in the range $0.005 - 0.1 \text{ cm}^{-3}$, EDE density close to the red giant n_{ede} in the range $10^7 - 5 \times 10^8 \text{ cm}^{-3}$, and characteristic length scale¹ h_z in the range 1–7 au (see Table 1). The model neglects the wind velocity ($\approx 10 \text{ km s}^{-1}$; e.g. Banerjee et al. 2014) which is expected to be several orders of magnitude lower than the velocity of the blast (much larger than 1000 km s^{-1}). We consider also additional simulations without an EDE and assuming the origin of the blast wave to be either coincident with the origin of the wind or offset from it by 1.7 au. The former models are analogous to the 1D models used by Drake et al. (2016) to interpret the *Chandra* data and are considered here just to compare our results with those of Drake et al. (2016), whereas the latter models highlight the effect of shielding of the blast by the red giant secondary.

For these additional simulations, we adopt blast and wind parameters consistent with those discussed by Drake et al. (2016). The explosion and subsequent expansion of the blast wave is followed for a total of 20 days in order to explore the evolution of the X-ray emission till the epoch of *Chandra* observations and study the effects of the circumstellar environment on the evolution of the blast.

Given the four-fold symmetry of the system, the hydrodynamic equations are solved in one quadrant of the whole spatial domain in order to reduce the computational cost. The coordinate system is oriented in such a way that both the white dwarf and the companion star lie on the x -axis (see Fig. 1). The companion is at the origin of the coordinate system, $(x, y, z) = (0, 0, 0)$, and the computational domain extends to 120 au in the x direction and 60 au in both the y and z directions; the white dwarf is located to the right on the x -axis ($y = z = 0$) at $x = 1.7$ au (namely the assumed binary separation; see Table 1). We impose reflecting boundary conditions at $y_{\min} = 0$ and $z_{\min} = 0$ (consistently with the adopted symmetry) and outflow (zero-gradient) conditions at the other boundaries.

As with previous modeling of other nova blasts (e.g. RS Oph, Walder et al. 2008; Orlando et al. 2009; U Sco, Drake & Orlando 2010; and V407 Cyg, Orlando & Drake 2012; Pan et al. 2015), the small scale of the stellar system compared with the size of the rapidly expanding blast wave over the period covered presents a major computational challenge. To this end, we exploit the adaptive mesh capabilities of FLASH by using 10 nested levels of adaptive mesh refinement, with resolution increasing twice at each refinement level. The refinement/derefinement criterion adopted (Löhner 1987) follows the changes in mass density, temperature, and tracer of ejecta. The calculations are performed using an automatic mesh derefinement scheme in the whole spatial domain except in the portion including the companion (where we keep the same resolution of ≈ 0.015 au during the whole evolution, corresponding to ≈ 40 grid points per radius of the companion). This strategy keeps the computational cost approximately constant as the blast expands (e.g. Orlando et al. 2015, 2016): the maximum number of refinement levels used in the calculation gradually decreased from 10 (initially) to 6 (at the end) following the expansion of the blast. At the beginning (at the end) of the simulations, this grid configuration yielded an effective resolution of ≈ 0.015 au (≈ 0.24 au) at the finest level, corresponding to ≈ 20 zones per initial radius of the remnant (> 150 zones per final radius of the remnant). The effective mesh size varied from $4096 \times 2048 \times 2048$ initially to $512 \times 256 \times 256$ at the end of the simulation.

From the model results, we synthesize the X-ray emission arising from the interaction of the blast wave with the surrounding medium. To this end, we adopt the Astrophysical Plasma Emission Code (APEC)² for optically-thin, collision-dominated plasma with solar abundances of Anders & Grevesse (1989) (AG). We assume abundances of 0.5 times the solar values for the wind and EDE (Orio et al. 2015), and AG abundances enhanced by a factor of 10 for the ejecta. The latter choice was guided by the evidence of metal-rich ejecta - with abundances enhanced by possibly

¹ We keep the values of the other length scales fixed, namely $h_x = h_y = 54$ au.

² <http://www.atomdb.org/>

Table 1. Adopted parameters and initial conditions for the hydrodynamic models of the 2014 V745 Sco explosion

Parameter	Value		Notes				
Secondary star radius	$R_* = 126 R_\odot$		Schaefer (2009)				
Binary separation	$a_{bs} = 1.7$ au		Schaefer (2009)				
Distance	$D = 7.8$ kpc		Schaefer (2010)				
Spatial domain	$-50 \leq x \leq 70$ au						
	$0 \leq y \leq 60$ au						
	$0 \leq z \leq 60$ au						
AMR max. resolution	2.25×10^{11} cm (0.015 au)						
Time covered	0–20 days						
Model abbreviation	E_b [erg]	M_{ej} [M_\odot]	n_w [cm $^{-3}$]	n_{ede} [cm $^{-3}$]	h_x [au]	h_y [au]	h_z [au]
E43-M7-W0.1-nostar	10^{43}	10^{-7}	0.1	—	—	—	—
E43.5-M7-W0.1-nostar	3×10^{43}	10^{-7}	0.1	—	—	—	—
E43-M7-W0.1	10^{43}	10^{-7}	0.1	—	—	—	—
E43.3-M7-W0.1	2×10^{43}	10^{-7}	0.1	—	—	—	—
E43-M7-H1-D8	10^{43}	10^{-7}	0.005	10^8	54	54	1
E43-M7-H2-D8	10^{43}	10^{-7}	0.005	10^8	54	54	2
E43-M7-H2-D8.7	10^{43}	10^{-7}	0.005	5×10^8	54	54	2
E43.3-M7-H2-D8	2×10^{43}	10^{-7}	0.005	10^8	54	54	2
E43.5-M6.5-H3-D8	3×10^{43}	3×10^{-7}	0.005	10^8	54	54	3
E43.5-M6.5-H3-D7.7	3×10^{43}	3×10^{-7}	0.005	5×10^7	54	54	3
E43.5-M6.5-H7-D7	3×10^{43}	3×10^{-7}	0.005	10^7	54	54	7
E43.5-M6-H3-D8	3×10^{43}	10^{-6}	0.005	10^8	54	54	3
E44-M6.5-H3-D7.7	10^{44}	3×10^{-7}	0.005	5×10^7	54	54	3
E44-M6.5-H3-D8	10^{44}	3×10^{-7}	0.005	10^8	54	54	3
E44-M6.5-H7-D7	10^{44}	3×10^{-7}	0.005	10^7	54	54	7

more than a factor of 10 - in high-resolution X-ray spectroscopic studies of RS Oph and V407 Cyg (e.g. Drake et al. 2009; Shore et al. 2011). The adopted abundances are important for the estimate of local absorption by the CSM and ejecta encountered within the blast wave and for the synthesis of X-ray emission arising from the blast. We adopt the methodology described by Orlando et al. (2009) to synthesize the X-ray emission. The latter includes the Doppler shift of lines due to the component of plasma velocity along the line of sight and the photoelectric absorption by the interstellar medium (ISM), CSM and ejecta. The absorption is computed using the absorption cross sections as a function of wavelength from Balucinska-Church & McCammon (1992). The local absorption is calculated self-consistently from the distributions of CSM and ejecta; the interstellar absorption is calculated assuming a neutral hydrogen column density of $N_H = 5 \times 10^{21}$ cm $^{-2}$ in agreement with suggestions from the analysis of *Chandra* and *Swift* observations (Page et al. 2015; Drake et al. 2016). A distance of 7.8 kpc is adopted in agreement with Schaefer (2010). The exposure time relevant for capturing the appropriate “blurring” of the explosion over the finite observation duration is assumed to be $t_{exp} = 40$ ks (roughly the same order of magnitude of observations by the *Chandra* High Energy Transmission Grating Spectrometer, HETG; Drake et al. 2016).

3 RESULTS

3.1 Hydrodynamic evolution

Our model predicts an evolution of the blast wave which is analogous to those found for other nova outbursts (Walder et al. 2008; Orlando et al. 2009; Drake & Orlando 2010; Orlando & Drake 2012; Pan et al. 2015). In V745 Sco, the white dwarf is located within the dense wind of its red giant secondary, as in the case of RS Oph and similar to the white dwarf of V407 Cyg which sits in the massive circumstellar gas envelope of its Mira companion. In particular, available information suggests that V745 Sco is probably analogous to the RS Oph system, having very similar values for the binary separation (between 1.5 and 1.7 au), the orbital period (of the order of 500 days), and the secondary star radius (between 120 and 150 R_\odot) (e.g. Dobrzycka & Kenyon 1994; Fekel et al. 2000; Schaefer 2009, 2010). In both systems the estimated mass accretion rate is of the order of $\approx 10^{-7} M_\odot$ yr $^{-1}$ (e.g. Kantharia et al. 2016). On the other hand, V745 Sco has a much tighter orbital separation than V407 Cyg, implying that, in the case under study, the nova explodes initially into a relatively higher density environment. The fact that the white dwarf of V745 Sco is very close to the companion (with an orbital separation of 1.7 au) together with the significant size of the companion ($R_* \approx 126 R_\odot \approx 0.6$ AU), implies that the red giant is expected to shield partially the blast, in analogy with the results found for the other novae.

Fig. 2 illustrates six representative simulations reproducing the blast wave evolution of V745 Sco. In particular, the figure shows the gas density distributions in the (x, z)

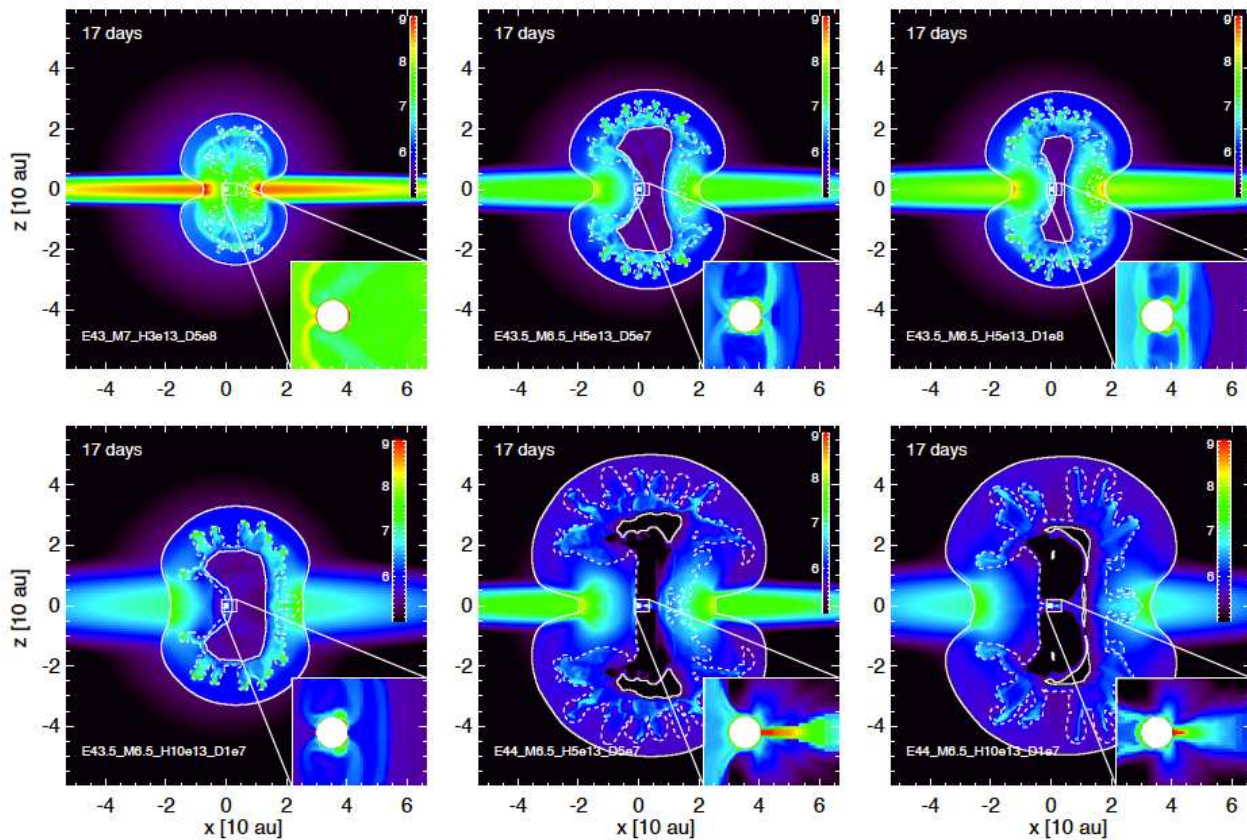


Figure 2. Cross-section images of the gas density distribution, on a logarithmic scale in units of cm^{-3} (see the colour table in the upper right-hand corner of each panel), at $t = 17$ days since the outburst, for six representative V745 Sco models. The red giant secondary is at the origin and the initial blast wave is offset from the origin to the right by 1.7 au. Inset panels show the blast structure in the immediate vicinity of the binary system. The white circle in the inset represents the red giant companion. The white dashed contour encloses the ejecta. The white solid contours denote the regions with plasma temperature $T > 10^5$ K: the outer solid contour marks the position of the forward shock, the inner one the position of the reverse shock.

plane bisecting the system (the equatorial plane is observed edge-on) at $t = 17$ days, roughly the time when the blast wave was observed by the *Chandra* X-ray observatory. The distribution of ejecta is delineated by the dashed contour which encloses regions where more than 90 per cent of the mass is material ejected in the explosion. As an example, a movie showing the 3D rendering of ejecta density (in units of cm^{-3}) and plasma temperature (in units of K) distributions during the blast evolution for model E43.5-M6.5-H3-D8 is provided as on-line material³ (movie 1). In all the cases examined, the system evolution is characterized by the fast expansion of the shock front with temperatures of a few millions degrees, and the development of Rayleigh-Taylor (RT) instabilities at the interface (contact discontinuity) between shocked ejecta and shocked ambient medium (e.g. Kane et al. 1999). In particular, the RT instabilities are

responsible for the growth of high density fingers extending towards the remnant outline (see Fig. 2 and movie 1). The inner (unshocked) ejecta are cool due to their fast adiabatic expansion. At this stage, thermal conduction rather than radiative cooling dominates the evolution of the shock heated plasma. As a result, both hydrodynamic and thermal instabilities that would otherwise develop during the blast expansion are significantly suppressed (e.g. Orlando et al. 2005, 2008).

Our simulations show aspherical shock morphologies rendered by the blast wave propagation through the inhomogeneous circumstellar environment, similar to those found from the modeling of the RS Oph and V407 Cyg outbursts (Walder et al. 2008; Orlando et al. 2009; Orlando & Drake 2012; Pan et al. 2015). In particular, the presence of a disc-like EDE leads to a characteristic bipolar shock morphology in which both the blast and the ejecta are strongly collimated in polar directions. The collimation is more prominent for lower explosion energy and/or higher density of EDE (e.g. runs E43-M7-H2-D8.7 and E43.5-M6.5-H3-D7.7 in Fig. 2) as might be expected. Fig. 3 shows, as an example, the collimation of ejecta 17 days after the outburst for the model E43.5-M6.5-H3-D8. Similar blast collimation but due to the presence of a dense circumstellar accretion

³ The blue volume in the movie is the unshocked EDE with density larger than 10^7 cm^{-3} , the orange sphere represents the red giant companion, and the white sphere offset to the right by 1.7 au the initial blast. Note that the original spatial resolution of the numerical data has been reduced to save memory when producing the movie describing the full evolution of the blast in the whole domain.

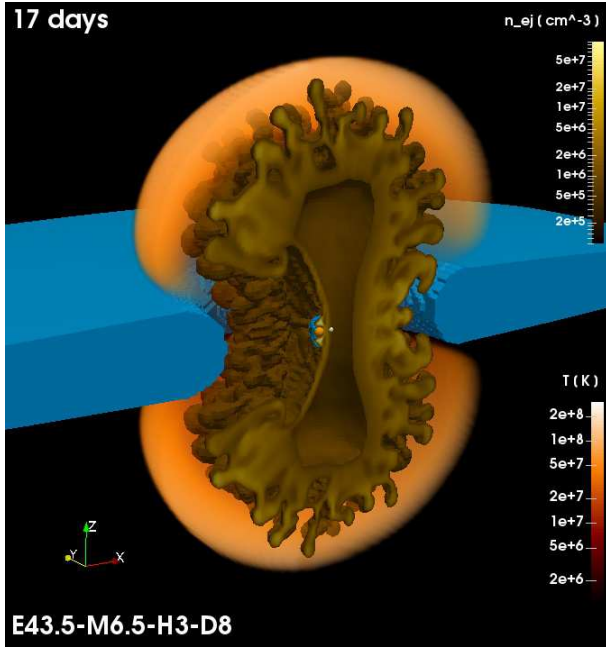


Figure 3. 3D rendering of the distributions of ejecta density (in units of cm^{-3}) and plasma temperature (in units of K), 17 days after the outburst for the model E43.5-M6.5-H3-D8. The volume has been sliced in the (x, z) plane bisecting the system for easy inspection of the blast interior. The blue volume is the unshocked EDE with density larger than 10^7 cm^{-3} , the orange sphere at the center of the domain represents the red giant companion, the white sphere offset to the right by 1.7 au the initial blast. The plane of the orbit of the central binary system lies on the (x, y) plane. Refer to on-line movie 1 for an animation of these data.

disc was predicted by hydrodynamic simulations of the early U Sco blast by Drake & Orlando (2010). The simulations also show that a reverse shock develops quite early in the evolution as a result of the interaction of the blast wave with the dense EDE. The reverse shock travels back into the expanding ejecta, heating them to temperatures of few MK (lower than the temperature of shocked CSM). We expect, therefore, that shocked ejecta contribute mainly to X-ray emission at longer wavelengths.

The shape of the blast is also affected by the presence of the red giant companion. The evolution is similar in all our simulations and Fig. 4 shows, as an example, the case of run E43.5-M6.5-H3-D8⁴. In fact, the shock front propagating towards the companion is partially shielded and refracted around it. Then the shock follows an evolution analogous to that found in hydrodynamic simulations of U Sco and V405 Cyg: the shock engulfs the companion star and converges on the rear side of it, undergoing a conical self-reflection (see lower panel in Fig. 4). At the same time, a

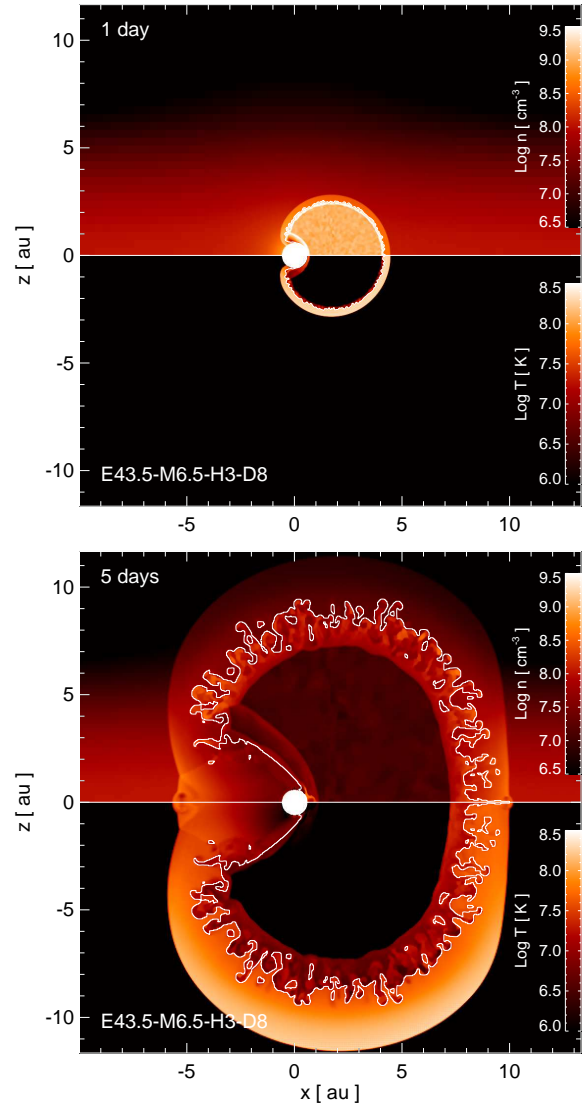


Figure 4. Close-up view of the cross-section images of the gas density distribution (upper half-panel) and temperature (lower half-panel) on a logarithmic scale (see color tables on the right of each panel), at the labeled times for run E43.5-M6.5-H3-D8. The white circle at the origin represents the red giant companion; the white solid contour encloses the ejecta.

bow shock with temperatures of few MK and density of $\approx 10^8 \text{ cm}^{-3}$ is produced on the front side of the companion, reheating the ejecta and contributing to their collimation in polar directions. As expected the bow shock is more energetic in models with the highest explosion energy (e.g. runs E44-M6.5-H3-D7.7 and E44-M6.5-H7-D7 in Fig. 2). In these cases, the interaction of the shock with the expanding unshocked ejecta leads to the formation of a dense region on the front side of the red giant (see lower center and right panels in Fig. 2).

From the simulations, we derive the distribution of emission measure vs temperature of the blast wave in order to compare our model results with those obtained from the analysis of *Chandra* observations (Drake et al. 2016). From the spatial distribution of mass density, we first derive the

⁴ An on-line movie shows a close up view of the 3D rendering of ejecta density (in units of cm^{-3}) and plasma temperature (in units of K) distributions during the early evolution of the blast wave for model E43.5-M6.5-H3-D8 (movie 2). The blue volume is the unshocked EDE with density larger than 10^8 cm^{-3} (the plane of the orbit lies on the (x, y) plane) and the orange sphere represents the red giant companion. Movie 2 shows the evolution of the blast at full spatial resolution.

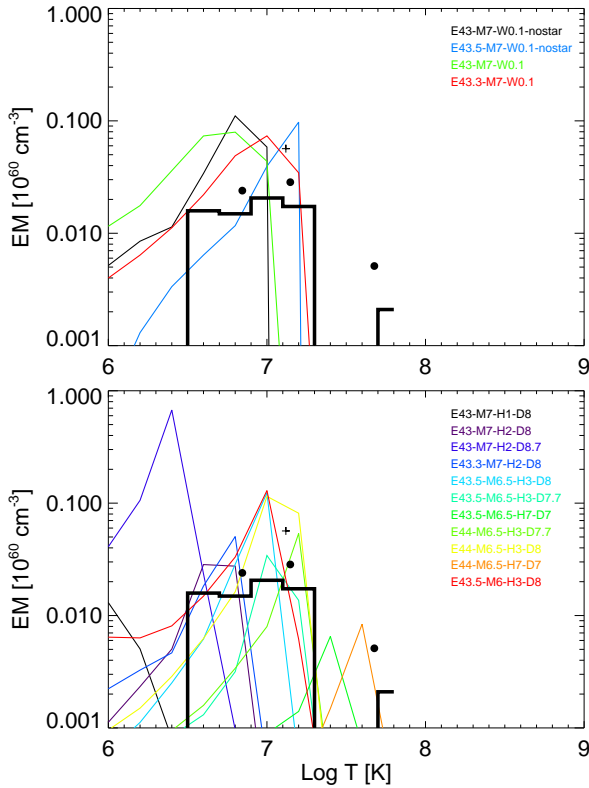


Figure 5. Emission measure vs temperature distributions, $EM(T)$, of the blast wave at day 17 derived from models either without (upper panel) or with (lower) EDE (see Table 1). The black histogram and the data points represent the $EM(T)$ estimated from the analysis of *Chandra*/HETG observations with an eight-temperature model fit (histogram), with a three-temperature model fit (black dots), and with an isothermal model fit (crosses) (Drake et al. 2016). The factor 10^{60} assumes a distance for V745 Sco of 7.8 kpc.

emission measure in the j -th domain cell as $em_j = n_{Hj}^2 V_j$, where n_{Hj}^2 is the hydrogen number density in the cell, V_j is the cell volume, and we assume fully ionized plasma. The $EM(T)$ distribution is then derived by binning the emission measure values as a function of temperature; the range of temperature [$6 < \log T(K) < 9$] is divided into 15 bins, all equal on a logarithmic scale. Figure 5 shows the $EM(T)$ for models either without (upper panel) or with (lower panel) EDE at day 17. The figure also shows the $EM(T)$ inferred from the analysis of *Chandra*/HETG spectra (Drake et al. 2016).

All the models (either with or without the EDE) show a similar trend of the $EM(T)$ distribution. The shape is characterized by a bump centered at temperatures between 10^6 and 10^8 K, depending on the parameters of the blast and CSM. The peak of EM is at higher temperatures for higher values of the explosion energy, E_0 , and/or for lower values of density of the EDE, n_{ede} . The peak of EM increases for higher values of EDE density, n_{ede} , and/or for higher mass of ejecta, M_{ej} . Models without EDE require a high density of the red giant wind, n_w , in order to fit the EM inferred from the observations at $T \approx 10^7$ K. Models including an EDE require a less dense wind and predict that the shape of $EM(T)$ depends on the thickness of the EDE. Among these,

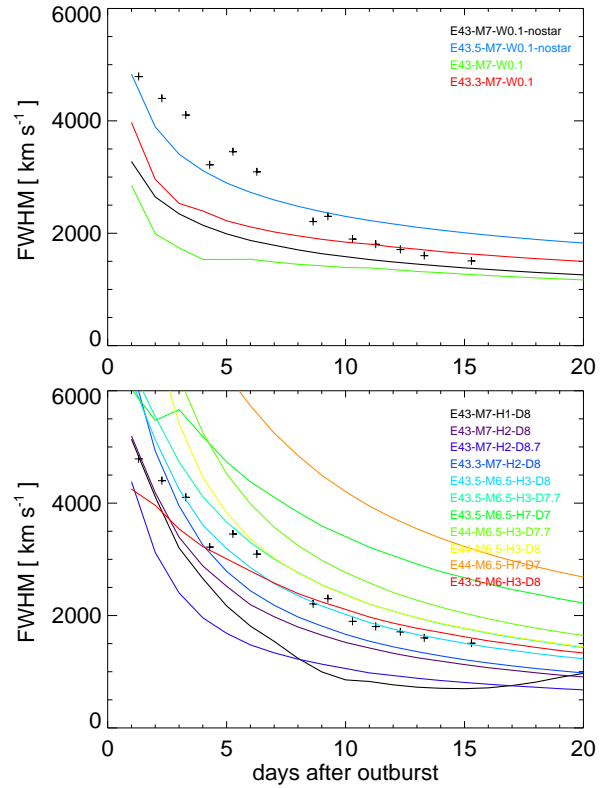


Figure 6. FWHM of H I Pa β emission line vs. time predicted by models either without (upper panel) or with (lower) EDE (see Table 1). The data points (crosses) represent the values inferred from observations of V745 Sco (Banerjee et al. 2014). The data points correspond to the broader line component in the line widths of Banerjee et al. (2014) which is interpreted as arising from the forward shock.

the models best matching the observed $EM(T)$ are those with explosion energy E_b between 3×10^{43} and 10^{44} erg, ejecta mass M_{ej} between 3×10^{-7} and $10^{-6} M_\odot$, EDE density n_{ede} between 5×10^7 and 10^8 cm^{-3} , and thickness of the EDE $h_z \approx 3$ au.

We note that, apparently, the $EM(T)$ inferred from the observations is characterized by two peaks, one centered at $T \approx 10^7$ K and the other at $T \approx 5 \times 10^7$ K. Our models are able to reproduce only the low temperature peak. From the analysis of *Chandra* observations of the 2006 outburst of RS Oph, Drake et al. (2009) noted that EM values at high temperatures may be influenced by effects of non-equilibrium ionization (NEI). However, the highest temperature is mainly determined by the continuum in the fits of observed spectra of V 745 Sco. The continuum shape follows the electron temperature and, in fact, Drake et al. (2016) have found that the fit to *Chandra* HETG looks really good out to the shortest wavelengths (see Fig. 3 of Drake et al. 2016). The Fe XXV ($\lambda 1.85$) line appears to be slightly underpredicted by the spectral model, suggesting that Fe ions might suffer from NEI effects. It is also possible that the hot plasma is a vestige of the super-hot ($T > 4 \times 10^7$ K) plasma observed in the first three days of the outburst by *Swift* (Page et al. 2015). Our models cannot describe this super-hot component and, in fact, they predict shock tem-

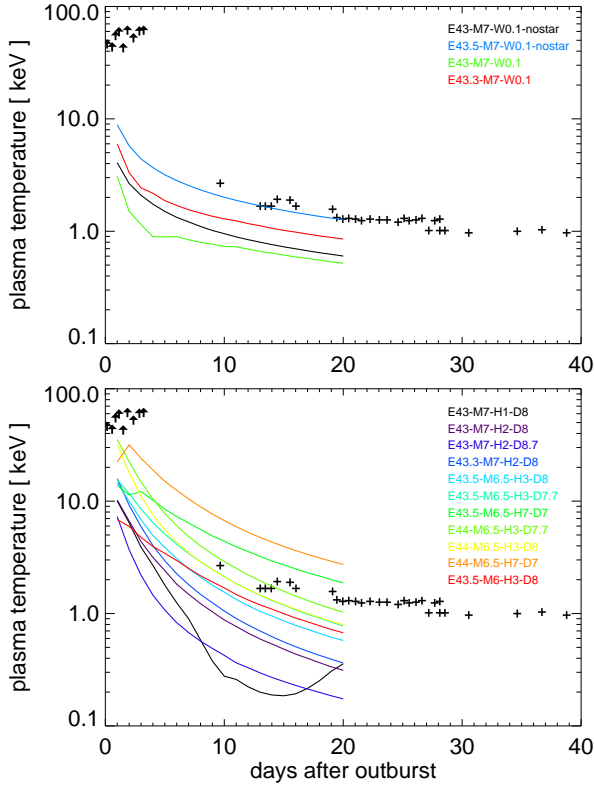


Figure 7. Average plasma temperature vs. time for the V745 Sco blast wave predicted by models either without (upper panel) or with (lower) EDE (curves; see Table 1) and those inferred from the analysis of *Swift* X-ray Telescope observations (crosses and arrows; Drake et al. 2016). The arrows at early times indicate lower limits to the temperature.

peratures significantly lower than those observed during the first few days, even with the EDE.

In order to constrain better the model parameters, we compare the evolution of average velocity and temperature of the blast derived from the simulations with those inferred from observations. In particular Banerjee et al. (2014) analyzed the profile of H I Pa β emission line between day 1 and 16 after outburst and found that, in general, the line is composed of broad and narrow components. Following Drake et al. (2016), we interpret the broad component as arising from the forward shocks, so that its full width at half maximum (FWHM) should reflect the average velocity of the blast (Banerjee et al. 2014; see Fig. 6). The average temperature of the blast as a function of time was derived by Drake et al. (2016) from the analysis of *Swift* X-ray Telescope observations (see Fig. 7). From the simulations, we derive the velocity, $\langle v_{\text{sh}} \rangle$, and temperature, $\langle T_{\text{sh}} \rangle$, of the forward shock, both averaged over the whole remnant outline and weighted for the emission measure. Then the FWHM of the H I Pa β line is calculated as $1.8 \langle v_{\text{sh}} \rangle$ (see Sect. 5 in Drake et al. 2016).

The comparison between modeled and observed quantities is reported in Figs. 6 and 7. Our 3D models without EDE (upper panels in the figures) produce results analogous to those of Drake et al. (2016), based on a 1D analytic model (Laming & Hwang 2003), if the blast is centered on the ori-

gin of the wind (runs E43-M7-W0.1-nostar and E43.5-M7-W0.1-nostar). The figures show that the effect of shielding of the blast by the red giant secondary produces significant changes in the evolution of $\langle v_{\text{sh}} \rangle$ and $\langle T_{\text{sh}} \rangle$ (see runs E43-M7-W0.1 and E43.3-M7-W0.1). None of these models produce a satisfactory description of the observations.

Among the models including the EDE, run E43.5-M6.5-H3-D8 best matches the average blast velocity vs. time (but it underestimates the average blast temperature), whereas run E44-M6.5-H3-D7.7 is the one best matching the average blast temperature (but it overestimates the average blast velocity). On the other hand, by comparing the effective areas of *Chandra* and *Swift*, we note that the latter is more sensitive to emission from plasma at high temperature; in fact, the shock temperature inferred from *Swift* observations around day 17 is slightly higher than that inferred from the analysis of *Chandra* observations (see Drake et al. 2016). We argue therefore that *Swift* detects preferentially the hotter plasma in the blast, namely that which propagates in polar directions. A compromise between the above two models matching either the shock velocity or the temperature is given by run E43.5-M6.5-H3-D7.7 which slightly overestimates $\langle v_{\text{sh}} \rangle$ by $\approx 10\%$ and underestimates $\langle T_{\text{sh}} \rangle$ by $\approx 50\%$. The model with the highest ejecta mass ($M_{\text{ej}} = 10^{-6} M_{\odot}$) considered, E43.5-M6-H3-D8, fits reasonably well the average blast velocity (although it systematically underestimates $\langle v_{\text{sh}} \rangle$ during the first 5 days of evolution), but it underestimates the average blast temperature as run E43.5-M6.5-H3-D8. All these four models (runs E43.5-M6.5-H3-D8, E43.5-M6.5-H3-D7.7, E44-M6.5-H3-D7.7, E43.5-M6-H3-D8) fit the observed EM(T) distribution quite well (see Fig 5).

Finally, we note again that all the models underestimate (even by one order of magnitude) the early-time *Swift* temperatures, although models with EDE are closer to match than models without EDE (compare upper and lower panels in Fig. 7). This is mainly due to the early collimation of the blast by the EDE in polar directions (see Fig. 4) which makes the shock propagating poleward much hotter than the shock front in models without EDE. Our favored models with explosion energy $E_b \approx 3 \times 10^{43}$ erg (namely runs E43.5-M6.5-H3-D8 and E43.5-M6.5-H3-D7.7) predict early temperatures of ≈ 20 keV, more than a factor of 2 lower than observed. A better match is obtained by models assuming an explosion energy $E_b \approx 10^{44}$ erg although, also in this case, the temperatures decay very quickly (at odds with observations) due to the fast adiabatic expansion of the blast. Presumably models with an even larger explosion energy might reproduce the observed values. However high explosion energies do not seem to be realistic in the present case and these models are expected to fail in reproducing the evolution of shock velocity.

3.2 X-ray emission and spectral line profiles

From the model results, we synthesize the X-ray emission in the [0.6 – 12.4] keV band using the method outlined in Section 2 (see also Orlando et al. 2009 for more details). Figs. 8 and 9 show maps of X-ray emission projected along the line of sight at day 17 (namely the time of *Chandra* observations; Drake et al. 2016) for the models reported in Fig. 2. Since the binary inclination remains unknown, in order to

explore the observational consequences of different inclinations we assume an inclination of the orbital plane relative to the sky plane either of 65° (Fig. 8) or of 25° (Fig. 9). The white dashed contours in the figures outline the ejecta projected along the line of sight. For high inclination of the binary orbit ($i = 65^\circ$), we find that, in general, most of the X-ray emission originates from the interaction of the blast with the EDE and is concentrated on the equatorial plane. Due to projection effects, the emission appears either in the form of small-scale sources propagating in the direction perpendicular to the line-of-sight (e.g. run E43-M7-H2-D8.7 in the upper left panel of Fig. 8) or as a ring-like structure lying in the equatorial plane (e.g. run E43.5-M6.5-H3-D8 in the upper right panel of Fig. 8). Similar plasma structures have been found in numerical simulations describing other nova outbursts (e.g. Walder et al. 2008; Orlando et al. 2009; Orlando & Drake 2012) and are generally expected as a result of the propagation of the blast through the EDE. In other cases, a smaller contribution to X-ray emission arises also from the ejecta collimated in polar directions (e.g. run E44-M6.5-H7-D7 in the lower right panel of Fig. 8). In some cases the contribution from the ejecta is dominant (e.g. run E43.5-M6.5-H7-D7 in the lower left panel of Fig. 8) and the X-ray source is a polar cap propagating toward the observer (namely the portion of the blast less affected by local absorption from dense ejecta). For low inclination of the binary orbit ($i = 25^\circ$), the morphology of the X-ray source is almost ring-like⁵ (see Fig. 9). Note that the dashed contours in Fig. 9 outline the ejecta projected along the line of sight; for low inclination of the orbit the contours delineate the cross-section of ejecta located at large distances above (or below) the equatorial plane where they are more expanded (see Fig. 8). This may give the false impression that the emission originates from the ejecta.

The synthetic spectra of V745 Sco as predicted to be observed by the *Chandra* High Energy Grating (HEG) and Medium Energy Grating (MEG) are derived by integrating the emission of the whole spatial domain. Synthetic line profiles include instrumental broadening which becomes a more significant component of the line profiles toward shorter wavelengths. The synthetic spectra are characterized by prominent emission lines from different elements, covering a large range in plasma temperature. This was expected on the basis of the EM(T) distributions derived from the models, revealing the broad nature of the plasma temperature distribution (see Fig. 5). We analyze the synthetic spectra with the aim to investigate the origin of the broadening and asymmetries detected in the observations by the *Chandra*/HETG (Drake et al. 2016). In particular, we restrict our analysis to the line profiles of the most prominent spectral lines reported in Table 2. We find that the model best reproducing the line profiles of V745 Sco observed with *Chandra* at days 16 and 17 is run E43.5-M6.5-

Table 2. Parameters (in units of $[\text{km s}^{-1}]$) characterizing the profiles of the most prominent spectral lines in the HEG and MEG spectra derived from *Chandra* observations and from run E43.5-M6.5-H3-D8, assuming different inclinations i of the orbital plane relative to the sky plane.

model E43.5-M6.5-H3-D8 assuming $i \approx 65^\circ$					
	v_{ctr}	FWHM	FWZI	BSZI	RSZI
S XVI ($\lambda 4.72$)	-25	1121	2902	-1476	1426
S XV ($\lambda 5.03$)	-5	1121	2882	-1446	1436
Si XIV ($\lambda 6.18$)	-35	1021	2652	-1366	1286
Si XIII ($\lambda 6.64$)	-35	960	2482	-1276	1206
Mg XII ($\lambda 8.42$)	-85	941	2332	-1256	1076
Mg XI ($\lambda 9.16$)	-95	910	2352	-1266	1086
Ne X ($\lambda 12.13$)	-225	940	2442	-1446	995
Fe XVII ($\lambda 15.01$)	-295	1011	2612	-1606	1006
O VIII ($\lambda 18.97$)	-405	1321	3423	-2117	1306
model E43.5-M6.5-H3-D8 assuming $i \approx 25^\circ$					
	v_{ctr}	FWHM	FWZI	BSZI	RSZI
S XVI ($\lambda 4.72$)	-15	880	2282	-1156	1126
S XV ($\lambda 5.03$)	15	850	2202	-1086	1116
Si XIV ($\lambda 6.18$)	-15	800	2082	-1056	1026
Si XIII ($\lambda 6.64$)	-5	700	1802	-905	895
Mg XII ($\lambda 8.42$)	-35	670	1761	-915	845
Mg XI ($\lambda 9.16$)	-35	650	1681	-875	805
Ne X ($\lambda 12.13$)	-145	910	2362	-1326	1036
Fe XVII ($\lambda 15.01$)	-575	1031	2682	-1916	765
O VIII ($\lambda 18.97$)	-1156	1981	5115	-3708	1506

H3-D8. For this model, Fig. 10 shows the profiles for the lines selected by Drake et al. (2016): the abundant H-like ions Si XIV ($\lambda 6.18$), Mg XII ($\lambda 8.42$), and Ne X ($\lambda 12.13$) observed by HEG and O VIII ($\lambda 18.97$) observed by the MEG⁶. The figure also compares the synthetic profiles with those observed with *Chandra* (Drake et al. 2016). Note that the signal-to-noise ratio is rather poor for the O VIII line. In the Appendix we report the line profiles derived for all the models shown in Figs. 8 and 9 and for the model with the highest ejected mass (E43.5-M6-H3-D8).

The synthetic lines exhibit broadening and asymmetries which are similar to those observed, especially if the plane of the orbit of the binary system is inclined by 65° (left panel in Fig. 10). These profiles are also similar to those predicted by hydrodynamic models describing the 2006 outburst of RS Oph (Orlando et al. 2009). We analyze the line profiles through fitting with a Gaussian function⁷. Table 2 reports the parameters characterizing the line profiles for our best-fit case: the shift of the line centroid v_{ctr} (negative values are for blue-shift), the full width at half maximum (FWHM),

⁵ Note that, in run E43-M7-H2-D8.7, the remnant morphology for a high inclination of the binary orbit ($i = 65^\circ$; see upper left panel of Fig. 8) is characterized by two small-scale sources instead of a ring-like structure (as for an inclination of $i = 25^\circ$; upper right panel of Fig. 9). This is due to heavy absorption of emission by the dense unshocked EDE for the proceeding portion of the remnant and by the dense unshocked ejecta for the receding portion of the remnant.

⁶ The O VIII ($\lambda 18.97$) doublet falls outside of the HEG range and is observed only by the MEG.

⁷ Note that, in many cases, a Gaussian function is only a rough approximation of the line profile, because the latter can be asymmetric and consisting of plasma components with different Doppler shift (see Fig. 10). Here the fit with a Gaussian component is intended just to provide indicative values of the line centroid and broadening.

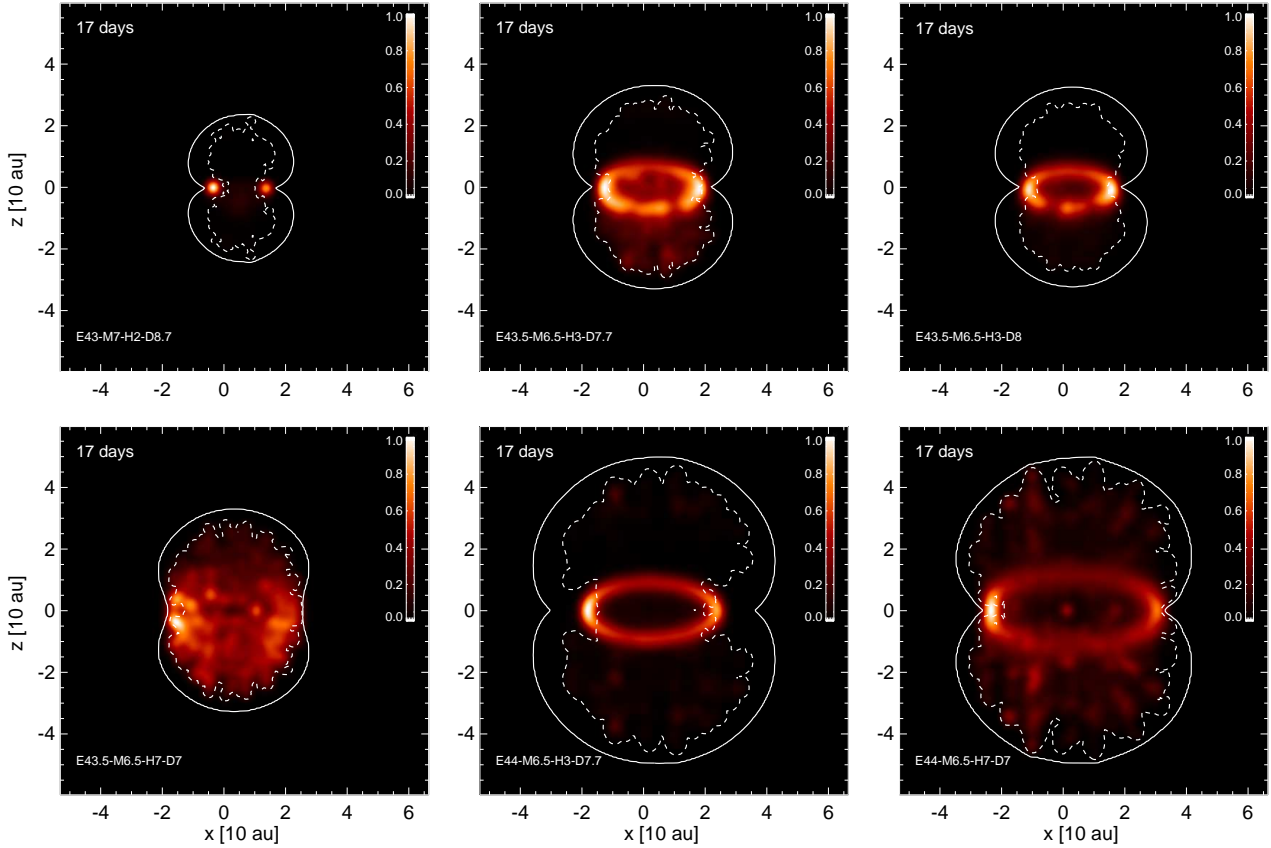


Figure 8. X-ray images of the blast (normalized to the maximum of each panel and in linear scale) in the $[0.6 - 12.4]$ keV band projected along the line of sight after 17 days of evolution, corresponding to the density distributions illustrated in Fig. 2. The plane of the orbit of the central binary system lies on the (x, y) plane and is assumed to be inclined by 65° relative to the sky plane. Note that, in this figure, z is the vertical axis in the inclined reference frame. The white dashed contour outlines the ejecta projected along the line of sight. The white solid contour denotes the projected forward shock.

the full width at zero intensity (FWZI), the line profile blue-shift at zero intensity (BSZI), and the line profile red-shift at zero intensity (RSZI). The values of the line widths include the instrumental broadening to make straightforward the comparison of model results with observations.

In velocity terms, the synthetic lines for the case with $i = 65^\circ$ are characterized by FWZI ranging between ≈ 2300 and 2900 km s^{-1} (except the O VIII line with FWZI of approximately 3400 km s^{-1}), FWHM ranging between ≈ 900 and 1100 km s^{-1} , more peaked than expected for a spherically-symmetric shock, and in agreement with *Chandra* observations. The lines are even more peaked assuming $i = 25^\circ$ (see Table 2). By comparing synthetic and observed line profiles in Fig. 10, we note that our most favoured model with $i = 65^\circ$ slightly underestimates the observed line widths for the Si XIV and Mg XII (left panels in the figure), whereas the Ne X line width is very well reproduced. The line fitting may be improved by changing slightly the inclination of the orbital plane relative to the sky plane. On the other hand, it is likely that the imperfect match of hotter lines is due to simplifications in the prescription of the EDE and CSM.

Drake et al. (2016) suggested that the pointed shape of emission lines indicates a highly collimated blast wave and have shown that line profiles similar to those observed can

be produced if the emission is restricted to an equatorial belt (ring-like) with a system inclination $i \approx 25^\circ$ or to one pole (cap-like) with $i \approx 85^\circ$. Our model predicts that most of the X-ray emission originates from the equatorial plane (see Figs. 8 and 9). In particular the models best matching the EM(T) distribution and the evolution of shock velocity and temperature inferred from the observations (runs E43.5-M6.5-H3-D7.7 and E43.5-M6.5-H3-D8) support the scenario of a prominent X-ray emitting equatorial ring, originating from the interaction of the blast with the EDE.

The centroids of the synthetic lines are, in general, blueshifted and the amount of the shift depends on the wavelength (see Table 2 and Fig. 10): assuming $i = 65^\circ$ the net blueshift increases from $\approx -25 \text{ km s}^{-1}$ in SXVI ($\lambda 4.72$) up to $\approx -400 \text{ km s}^{-1}$ in O VIII ($\lambda 18.97$) which is the most striking case. If we assume an inclination $i = 25^\circ$, again the blueshift increases with the wavelength but now the trend appears clear only for wavelengths larger than 9 \AA ; there the blueshift increases from $\approx -35 \text{ km s}^{-1}$ in Mg XI ($\lambda 9.16$) up to the very high value of $\approx -1100 \text{ km s}^{-1}$ in O VIII ($\lambda 18.97$). The result obtained for $i = 65^\circ$ is that best reproducing the result found from the analysis of *Chandra*/HETG observations. The line profiles tend to be more extended to the blue than the red, and the effect is most striking for the O VIII doublet (see Fig. 10). As noted by Drake et al.

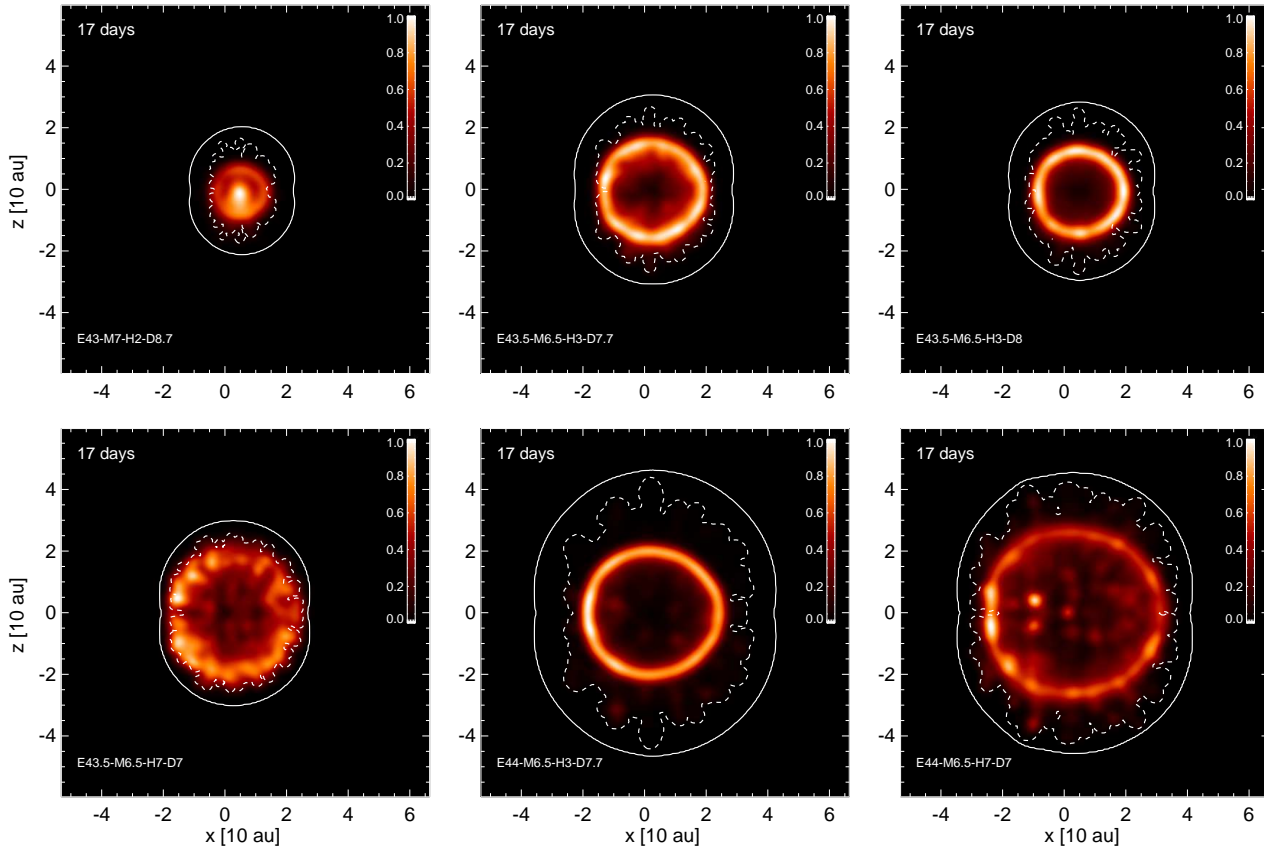


Figure 9. As in Fig. 8 but assuming the plane of the orbit of the central binary system to be inclined by 25° relative to the sky plane; z is the vertical axis in the inclined reference frame.

(2016), this pattern is a clear signature of intrinsic absorption within the remnant which affects mainly the emission from the shock heated plasma on the remnant hemisphere propagating away from the observer. Our simulations confirm that the prominent blueshift of synthetic lines is caused by the ejecta which mostly absorb the emission originating from the receding portion of the remnant that would otherwise contribute to the redshifted wing of the lines.

The tracer associated with the ejecta allows us to determine the contribution of shocked ejecta to the X-ray emission. Fig. 10 shows that the emission lines consist of two components: one due to shocked ejecta (red lines in the figure) and the other to shocked CSM (blue lines). The former increases for longer wavelengths: the emission of O VIII is almost entirely due to shocked ejecta. In fact, as discussed in Sect. 3.1, the interaction of the blast with the CSM triggers the development of a reverse shock which heats the ejecta to temperatures lower than that of shocked CSM (see Fig. 4). As a result, the dominant contribution to the X-ray spectrum at wavelengths shorter than ≈ 10 Å comes from the forward shock-heated CSM as expected during the early phase in symbiotic novae (e.g. Bode & Kahn 1985). This result is also in agreement with the findings of Drake et al. (2016) that the abundances derived from the analysis of *Chandra* spectra are consistent with a solar mixture. It is worth mentioning here that our results depend on the assumption of AG abundances enhanced by a factor of 10 for the ejecta. A change to the abundances of ejecta would al-

ter the balance of ejecta vs CSM contributions to emission lines. This is especially true for the Ne X line of our best-fit model in which the two contributions are comparable. On the other hand, for O VIII the ejecta are still expected to be a significant contributor even for solar-like abundances.

Due to the larger ejecta abundances, the redshifted emission from the ejecta is, in general, more absorbed than that of shocked CSM. As a consequence the ejecta component appears more asymmetric and blueshifted than the CSM component. Inspecting Fig. 8, we note that a contribution to emission may arise from shocked ejecta collimated in polar directions (e.g. runs E43.5-M6.5-H3-D7.7 and E44-M6.5-H7-D7 in the figure). The effect is most striking in run E43.5-M6.5-H7-D7 where the contribution from ejecta dominates (see also the Appendix). Due to the local absorption, the contribution to emission is the largest from the ejecta propagating toward the observer, so that a net blueshift is expected for this component (see the Appendix for a more detailed analysis of this case). A larger ejected mass makes the contribution of shocked ejecta to X-ray emission larger. This is the case, for instance, of run E43.5-M6-H3-D8 with $M_{\text{ej}} = 10^{-6} M_\odot$: the O VIII and Ne X lines are dominated by shocked ejecta (see the Appendix).

Indeed our simulations suggest that an accurate analysis of X-ray emission lines might reveal useful information about the chemical composition of the ejecta in these explosions. To do this, we need to disentangle the ejecta contribution to emission from the CSM contribution. This depends

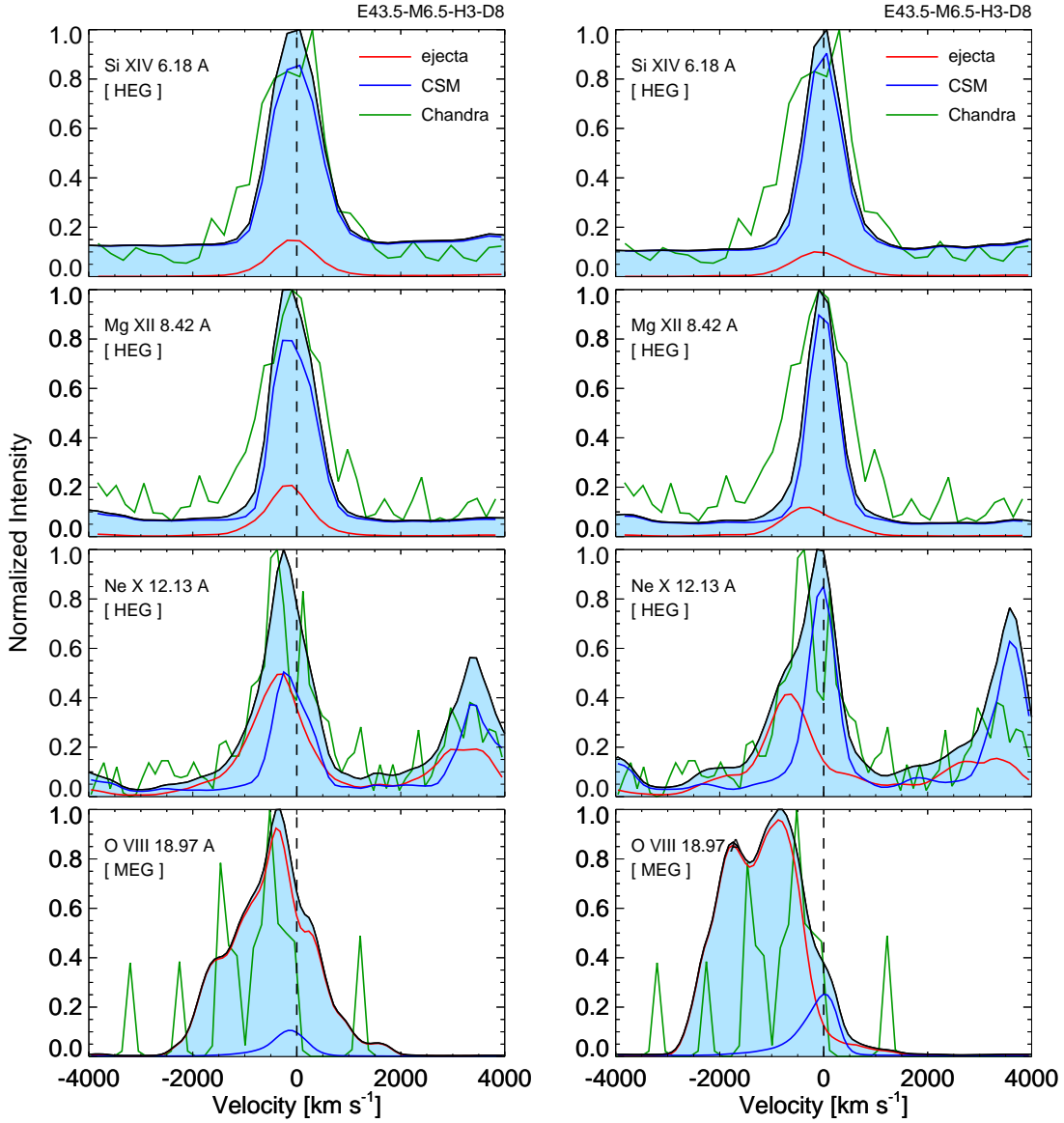


Figure 10. Synthetic velocity profiles of the H-like resonance lines of Si XIV, Mg XII, Ne X, and O VIII (shades lightblue) derived from model E43.5-M6.5-H3-D8 at day 17. The plane of the orbit of the central binary system lies on the (x, y) plane and is assumed to be inclined either by 65° (on the left) or by 25° (on the right) relative to the sky plane. The red and blue lines represent the contribution to X-ray emission of shocked ejecta material and shocked CSM, respectively. Line profiles observed with the *Chandra* HETG are superimposed (green lines; Drake et al. 2016).

on the quality of the collected spectra of course, but it critically depends also on the combination of explosion parameters and density distribution of the surrounding CSM. In the case of “cold” lines dominated by ejecta, the poor signal-to-noise ratio obtained for some of these lines (e.g. see the O VIII line in Fig. 10) can make difficult to derive information about the chemical composition of the ejecta. Nevertheless, in the case of V745 Sco under study, by comparing the predicted and observed Ne and O spectral line ratios, we find no signs of strong Ne enhancement that might betray a NeMgO white dwarf. Thus our model suggests that the progenitor white dwarf is a CO type.

In the case of hotter lines the ejecta contribution to the total line profile can be only a small percentage even

with abundances enhanced by a factor of 10; this is the case of Si and Mg in run E43.5-M6.5-H3-D8 but also of Ne in which the contribution from ejecta to the total line profile is only about 50% (see Fig. 10). On the other hand, we find also cases in which the X-ray emission may be dominated by shocked ejecta at all wavelengths (see the Appendix for more details). An example is run E43.5-M6.5-H7-D7 (see lower left panel in Fig. 8) in which the low density of the EDE makes the contribution of shocked CSM to emission smaller than that of shocked ejecta. Possibly, in these cases, we may hope to be able to detect ejecta enriched in the underlying white dwarf material from blast wave spectra. This would be valuable for determining more accurately whether the underlying white dwarf is a CO or an NeMgO type.

4 SUMMARY AND CONCLUSIONS

We investigated the origin of broadening and asymmetries of emission lines observed with *Chandra*/HETG during the 2014 outburst of V745 Sco. The analysis was performed through a 3D hydrodynamic model which describes the interaction of the blast wave from the outburst with the inhomogeneous CSM. The model takes into account simultaneously the radiative cooling and the thermal conduction, and considers an EDE surrounding the binary system.

We explored the parameter space of the model and found that, in all the cases, the blast wave is highly aspherical and its morphology is largely influenced by the pre-existing inhomogeneous CSM. Both the blast and the ejecta distribution are efficiently collimated in polar directions due to the presence of the EDE. In addition, the shock front propagating toward the red giant companion is partially shielded by it. As a result, depending on the explosion energy and density of the EDE, a wake with dense and hot post-shock plasma can form on the rear side of the companion star.

We searched for the model best fitting the observations by comparing the average velocity and temperature of the forward shock derived from the models with those inferred from observations. We found that the observations are best reproduced if the mass of ejecta in the outburst was $M_{\text{ej}} \approx 3 \times 10^{-7} M_{\odot}$ and the explosion energy was $E_b \approx 3 \times 10^{43}$ erg. This model predicts a distribution of emission measure vs. temperature and an evolution of shock velocity and temperature which are compatible with those derived from the analysis of observations, and our ejected mass and explosion energy assessments are broadly in agreement with the estimates of Banerjee et al. (2014) and Drake et al. (2016). Interestingly, an ejected mass of $\approx 3 \times 10^{-7} M_{\odot}$ is considerably lower than the mass needed to initiate the thermonuclear reaction (Drake et al. 2016). If true, then the conclusion is that the system will be gaining mass making V745 Sco a Type Ia supernova (SN1a) progenitor candidate.

Our best-fit model allowed us to constrain also the average density structure and geometry of the pre-nova environment: the binary system is surrounded by an EDE with density ranging between 5×10^7 and 10^8 cm^{-3} and thickness ≈ 3 au. This information is important in view of future studies concerning the origin of the non-thermal emission detected during the blast wave evolution in radio and γ -rays (Kantharia et al. 2016; Cheung et al. 2014, 2015). In particular the γ -rays likely originate in the interaction of the blast and ejecta with the immediate circumstellar environment (Ackermann et al. 2014; Chomiuk et al. 2014). The case of V745 Sco, where the γ -ray detection almost coincided with the nova onset, indicates a rapid particle acceleration and, therefore, suggests a very dense medium in the immediate vicinity of the white dwarf. This is consistent with expectations of the structure of the EDE that we have diagnosed here.

We synthesized the X-ray emission during the blast wave evolution and found that, in general, most of the X-ray emission originates from the interaction of the blast with the EDE and is concentrated on the equatorial plane. Due to projection effects, the emission appears either in the form of small-scale sources propagating in the direction perpendicular to the line-of-sight or as a ring-like structure. A con-

tribution to emission may arise also from the shocked ejecta collimated in polar directions. In this case the sources of X-ray emission are, in general, in the form of polar-caps. In all the cases, the synthetic line profiles are more peaked than expected for a spherically symmetric shock, in nice agreement with the observations.

As found from the analysis of *Chandra*/HETG observations (Drake et al. 2016), the synthetic line profiles are asymmetric and slightly blueshifted, especially at wavelengths larger than 7 Å. Our analysis shows that these asymmetries are due to substantial X-ray absorption of redshifted emission by ejecta material, confirming the conclusion of Drake et al. (2016). The X-ray emission lines consist of two components, one originating from the shocked CSM and the other from shocked ejecta. The former is the dominant contribution, at least for wavelengths shorter than ≈ 10 Å. The latter component suffers more the effect of local absorption of redshifted emission and exhibits the largest asymmetries. Our models indicate that, in general, shocked ejecta contribute substantially to both Ne X and O VIII lines (e.g. see Fig. 10). While there are still some discrepancies between models and observations, comparison of predicted and observed Ne and O spectral line ratios reveals no signs of strong Ne enhancement (see also the other cases discussed in the Appendix) that might betray a NeMgO white dwarf and suggests the progenitor is instead a CO white dwarf. Finally the model best matching the observed line profiles requires a high inclination of the orbital plane relative to the sky plane ($\approx 65^\circ$).

Our simulations confirm that the presence of an EDE or a disc-like structure around the white dwarf in these systems is an important ingredient in shaping the expanding blast wave and ejecta distribution and, thus, in determining the characteristics of the emitted spectra. Analogous results obtained from the modeling of other recurrent nova outbursts (RS Oph, U Sco, V407 Cyg) suggest that blast and ejecta collimation by an EDE is likely an ubiquitous feature in these systems. The results presented here point out once more that the analysis of X-ray spectra from nova outbursts together with accurate hydrodynamic modeling may provide information on the structure and geometry of the environment around these objects and, ultimately, useful clues to the late stages of stellar evolution.

ACKNOWLEDGMENTS

This work was partially funded by the PRIN INAF 2014 grant “Filling the gap between supernova explosions and their remnants through magnetohydrodynamic modeling and high performance computing”. SO thanks his father, Saverio Orlando, for always supporting him and pushing him towards his dreams. JJD was supported by NASA contract NAS8-03060 to the CXC and thanks the director, B. Wilkes, and the CXC science team for advice and support. The software used in this work was in part developed by the DOE-supported ASC/Alliance Center for Astrophysical Thermonuclear Flashes at the University of Chicago. The simulations were executed at the SCAN⁸ (Sistema di Cal-

⁸ http://www.astropa.unipa.it/progetti_ricerca/HPC/index.html

colo per l'Astrofisica Numerica) facility for high performance computing at INAF – Osservatorio Astronomico di Palermo (Italy). Finally we thank the anonymous referee whose comments enabled us to improve the paper.

REFERENCES

- Ackermann M., Ajello M., Albert A., Baldini L., Ballet J., Barbiellini G., Bastieri D., Bellazzini R., Fermi-LAT Collaboration 2014, *Science*, 345, 554
- Anders E., Grevesse N., 1989, *Geochim. Cosmochim. Acta*, 53, 197
- Anupama G. C., Mikolajewska J., 1999, *Astron. & Astrophys.*, 344, 177
- Balucinska-Church M., McCammon D., 1992, *Astrophys. J.*, 400, 699
- Banerjee D. P. K., Joshi V., Venkataraman V., Ashok N. M., Marion G. H., Hsiao E. Y., Raj A., 2014, *Astrophys. J.*, 785, L11
- Bode M. F., Kahn F. D., 1985, *Mon. Not. R. Astron. Soc.*, 217, 205
- Bode M. F., O'Brien T. J., Osborne J. P., Page K. L., Senziani F., Skinner G. K., Starrfield S., Ness J.-U., Drake J. J., Schwarz G., Beardmore A. P., Darnley M. J., Eyres S. P. S., Evans A., Gehrels N., Goad M. R., Jean P., Krautter J., Novara G., 2006, *Astrophys. J.*, 652, 629
- Cheung C. C., Jean P., Shore S. N., 2014, *The Astronomer's Telegram*, 5879
- Cheung C. C., Jean P., Shore S. N., E. G. J., M. L., 2015, in *Proc. 34th ICRC, Gamma Ray Astronomy: Experimental Results (Trieste: SISSA)*, p. 880
- Chomiuk L., Linford J. D., Yang J., O'Brien T. J., Paragi Z., Mioduszewski A. J., Beswick R. J., Cheung C. C., Mukai K., Nelson T., Ribeiro V. A. R. M., Rupen M. P., Sokoloski J. L., Weston J., Zheng Y., Bode M. F., Eyres S., Roy N., Taylor G. B., 2014, *Nature*, 514, 339
- Colella P., Woodward P. R., 1984, *Journal of Computational Physics*, 54, 174
- Dobrzycka D., Kenyon S. J., 1994, *Astronom. J.*, 108, 2259
- Drake J. J., Delgado L., Laming J. M., Starrfield S., Kashyap V., Orlando S., Page K. L., Hernanz M., Ness J.-U., Gehr R. D., van Rossum D., Woodward C. E., 2016, *Astrophys. J.*, 825, 95
- Drake J. J., Laming J. M., Ness J.-U., Orlando S., Starrfield S., Beardmore A. P., Bode M. F., Evans A., Eyres S. P. S., Gehr R. D., Goad M. R., Gonzalez-Riestra R., Krautter J., O'Brien T. J., Osborne J. P., Page K. L., Schwarz G., Woodward C. E., 2009, *Astrophys. J.*, 691, 418
- Drake J. J., Orlando S., 2010, *Astrophys. J.*, 720, L195
- Duerbeck H. W., 1989, *The Messenger*, 58, 34
- Fekel F. C., Joyce R. R., Hinkle K. H., Skrutskie M. F., 2000, *Astronom. J.*, 119, 1375
- Fryxell B., Olson K., Ricker P., Timmes F. X., Zingale M., Lamb D. Q., MacNeice P., Rosner R., Truran J. W., Tufo H., 2000, *Astrophys. J. Suppl.*, 131, 273
- Kane J., Drake R. P., Remington B. A., 1999, *Astrophys. J.*, 511, 335
- Kantharia N. G., Dutta P., Roy N., Anupama G. C., Ishwara-Chandra C. H., Chitale A., Prabhu T. P., Banerjee D. P. K., Ashok N. M., 2016, *Mon. Not. R. Astron. Soc.*, 456, L49
- Kato M., Hachisu I., 1994, *Astrophys. J.*, 437, 802
- Kato M., Hachisu I., 2009, *Astrophys. J.*, 699, 1293
- Laming J. M., Hwang U., 2003, *Astrophys. J.*, 597, 347
- Löhner R., 1987, *Comp. Meth. Appl. Mech. Eng.*, 61, 323
- Luna G. J. M., Montez R., Sokoloski J. L., Mukai K., Kastner J. H., 2009, *Astrophys. J.*, 707, 1168
- Metzger B. D., Finzell T., Vurm I., Hascoët R., Beloborodov A. M., Chomiuk L., 2015, *Mon. Not. R. Astron. Soc.*, 450, 2739
- O'Brien T. J., Bode M. F., Porcas R. W., Muxlow T. W. B., Eyres S. P. S., Beswick R. J., Garrington S. T., Davis R. J., Evans A., 2006, *Nature*, 442, 279
- Orio M., Rana V., Page K. L., Sokoloski J., Harrison F., 2015, *Mon. Not. R. Astron. Soc.*, 448, L35
- Orlando S., Bocchino F., Reale F., Peres G., Pagano P., 2008, *Astrophys. J.*, 678, 274
- Orlando S., Drake J. J., 2012, *Mon. Not. R. Astron. Soc.*, 419, 2329
- Orlando S., Drake J. J., Laming J. M., 2009, *Astron. & Astrophys.*, 493, 1049
- Orlando S., Miceli M., Pumo M. L., Bocchino F., 2015, *Astrophys. J.*, 810, 168
- Orlando S., Miceli M., Pumo M. L., Bocchino F., 2016, *Astrophys. J.*, 822, 22
- Orlando S., Peres G., Reale F., Bocchino F., Rosner R., Plewa T., Siegel A., 2005, *Astron. & Astrophys.*, 444, 505
- Page K. L., Osborne J. P., Kuin N. P. M., Henze M., Walter F. M., Beardmore A. P., Bode M. F., Darnley M. J., Delgado L., Drake J. J., Hernanz M., Mukai K., Nelson T., Ness J.-U., Schwarz G. J., Shore S. N., Starrfield S., Woodward C. E., 2015, *Mon. Not. R. Astron. Soc.*, 454, 3108
- Pan K.-C., Ricker P. M., Taam R. E., 2015, *Astrophys. J.*, 806, 27
- Schaefer B. E., 2009, *Astrophys. J.*, 697, 721
- Schaefer B. E., 2010, *VizieR Online Data Catalog*, 218
- Shore S. N., Wahlgren G. M., Augusteijn T., Liimets T., Page K. L., Osborne J. P., Beardmore A. P., Koubsky P., Šlechta M., Votruba V., 2011, *Astron. & Astrophys.*, 527, A98+
- Sokoloski J. L., Luna G. J. M., Mukai K., Kenyon S. J., 2006, *Nature*, 442, 276
- Starrfield S., Truran J. W., Sparks W. M., 2000, *New Astronomy Review*, 44, 81
- Waagen E. O., 2014, *AAVSO Alert Notice*, 497
- Walder R., Folini D., Shore S. N., 2008, *Astron. & Astrophys.*, 484, L9

APPENDIX A: PROFILES OF X-RAY EMISSION LINES

In the paper we discuss in detail the synthetic line profiles as predicted to be observed by the *Chandra* HEG and MEG for our best-fit model, namely run E43.5-M6.5-H3-D8 (see Fig. 10 and Table 2). Here we report the line profiles of the abundant H-like ions Si XIV ($\lambda 6.18$), Mg XII ($\lambda 8.42$), Ne X ($\lambda 12.13$) and O VIII ($\lambda 18.97$) for the models shown in Figs. 8 and 9 (see Figs. A1-A6) and for the model with the highest ejected mass (E43.5-M6-H3-D8). We find that the models show significant differences in the synthetic line profiles de-

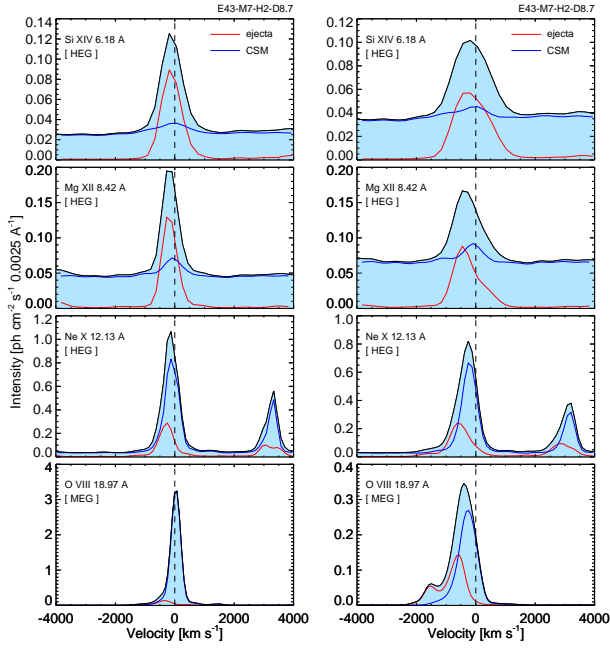


Figure A1. As in Fig. 10 for run E43-M7-H2-D8.7 (see also upper left panel in Figs. 8 and 9).

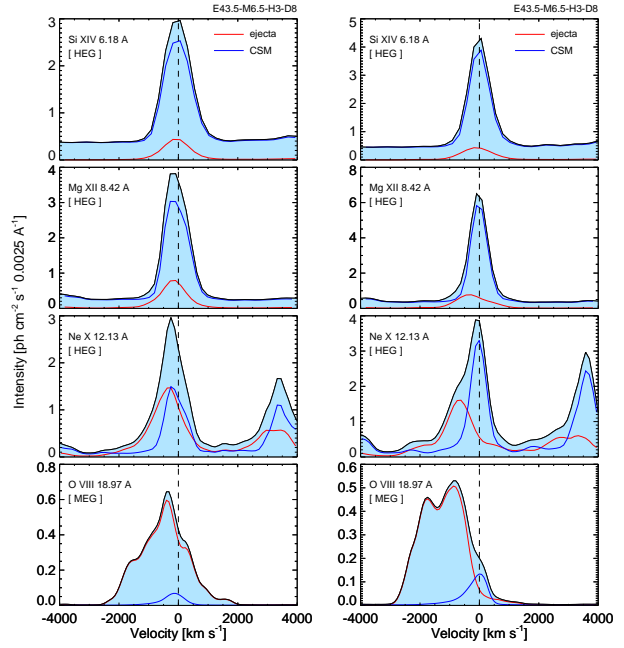


Figure A3. As in Fig. 10 for run E43.5-M6.5-H3-D8 (see also upper right panel in Figs. 8 and 9).

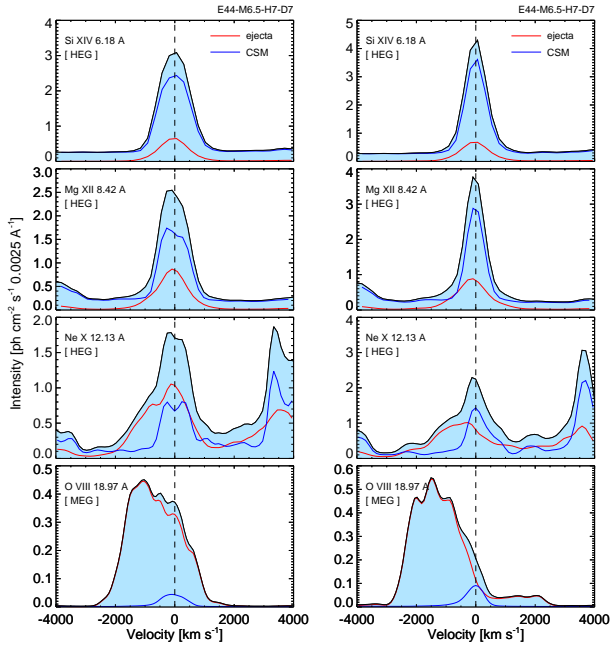


Figure A2. As in Fig. 10 for run E43.5-M6.5-H3-D7.7 (see also upper center panel in Figs. 8 and 9).

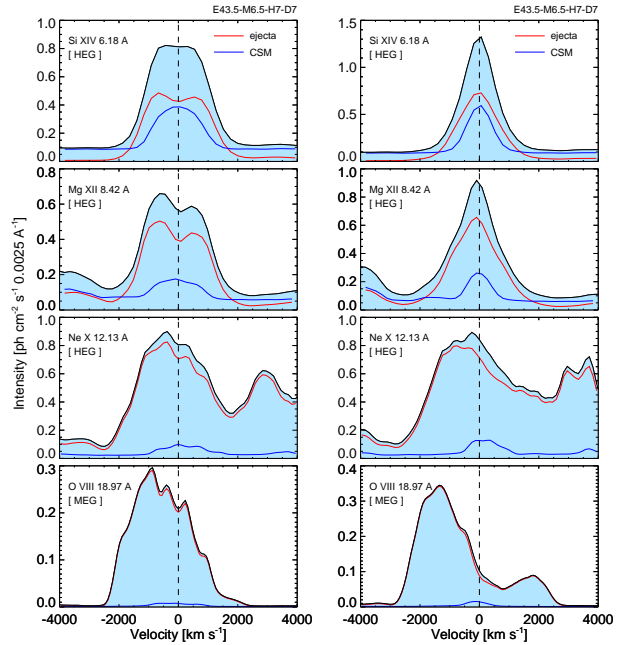


Figure A4. As in Fig. 10 for run E43.5-M6.5-H7-D7 (see also lower left panel in Figs. 8 and 9).

pending on the combination of explosion parameters and density distribution of the surrounding CSM.

In general, the emission is dominated by shocked CSM at shorter wavelengths and by shocked ejecta at longer wavelengths as found for run E43.5-M6.5-H3-D8. There are however two exceptions. In run E43-M7-H2-D8.7, the line profiles are very sharp and the emission is dominated by shocked ejecta at shorter wavelengths and by shocked CSM at longer wavelengths (see Fig. A1). This is mainly due to the high

density of the EDE which makes the reverse shock heating the ejecta stronger and the shocked CSM denser and colder than in other models. The result is that the shocked ejecta are hotter than the shocked CSM so that they contribute more to the emission of “hot” lines.

The other exception is run E43.5-M6.5-H7-D7 in which the main contribution to line emission originates from shocked ejecta for all the lines selected (see Fig. A4). Now the cause is the low density of the EDE which makes the

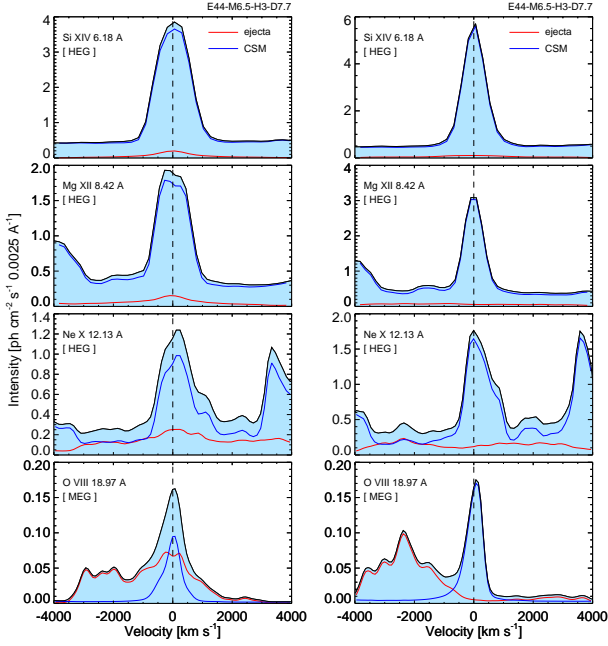


Figure A5. As in Fig. 10 for run E44-M6.5-H3-D7.7 (see also lower center panel in Figs. 8 and 9).

contribution to emission from shocked CSM smaller than that in the other models. We note also that, in this case, the line profiles may show two peaks (for instance in the Mg XII line in the left panel of Fig. A4) when the orbital plane is highly inclined relative to the sky plane (65°). This feature is the consequence of the collimation of shocked ejecta in polar directions, so that the sources of X-ray emission are polar-caps propagating one toward, and the other away from, the observer. As a result, the double-peaked lines reflect these two ejecta components, one blueshifted and the other redshifted, with the latter more absorbed by the dense ejecta and CSM placed along the line-of-sight.

Finally, the model with the highest ejected mass (E43.5-M6-H3-D8) present a significant contribution of shocked ejecta especially at longer wavelengths (see Fig. A7). This is not surprising because, in this case, the density of ejecta is higher than in our best-fit model E43.5-M6.5-H3-D8. Since the effect of local absorption is larger for the ejecta (due to their larger abundances), the redshifted emission from the ejecta is more absorbed than that of shocked CSM and the line profiles in run E43.5-M6-H3-D8 are more asymmetric and blueshifted than in run E43.5-M6.5-H3-D8 and in the observations (see Drake et al. 2016).

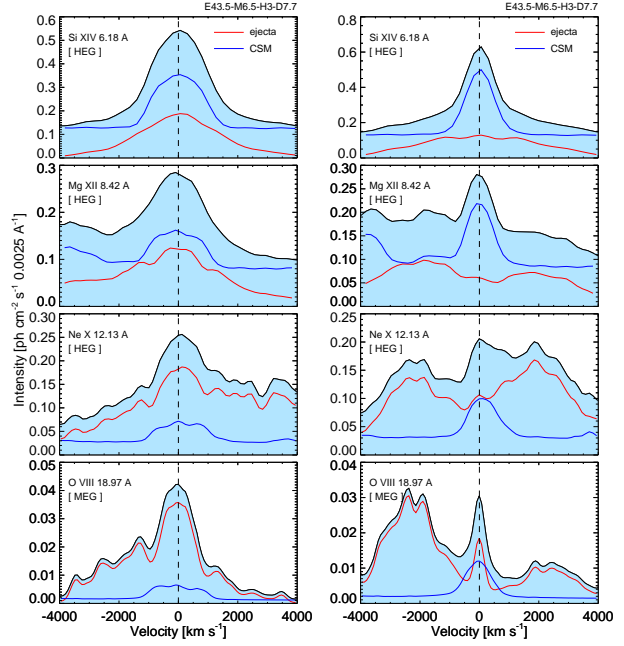


Figure A6. As in Fig. 10 for run E44-M6.5-H7-D7 (see also lower right panel in Figs. 8 and 9).

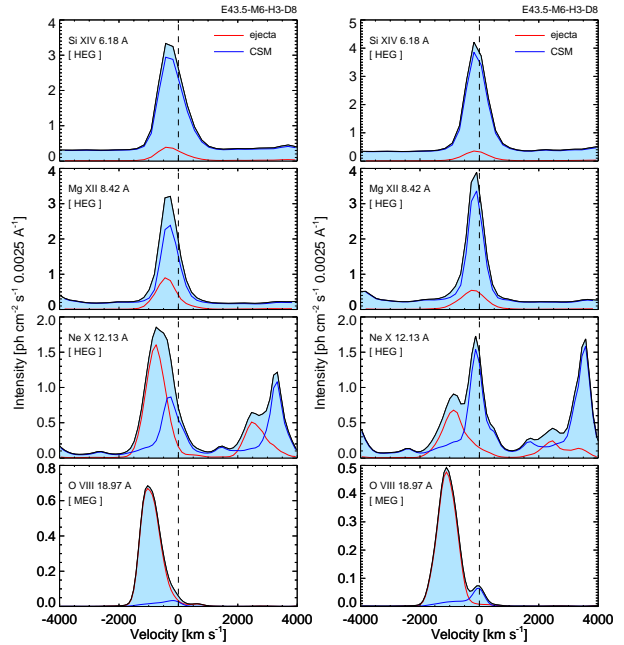


Figure A7. As in Fig. 10 for run E43.5-M6-H3-D8.